AISTech 2023 — Proceedings of the Iron & Steel Technology Conference
8–11 May 2023, Detroit, Mich., USA
DOI: 10.33313/387/217

In-Situ Observation of the Solidification of X70 Steel Using High-Temperature Confocal Scanning Laser Microscope

Katelyn Kiser*, Viraj A. Athavale, Laura Bartlett, Ronald O'Malley, Mario Buchely

Missouri University of Science and Technology
223 McNutt Hall, 1400 N. Bishop, Rolla, MO, 65401
Phone: (573)341-4711
*Email:kekmkq@mst.edu

Keywords: solidification, HT-CSLM, X70, line pipe steel, inclusions

INTRODUCTION

X70 is a microalloyed carbon-manganese high-strength steel commonly used in line pipe applications. Due to the increased economic appeal of transporting materials like petroleum derivatives through pipelines, there is a continued interest in improving the steels used in these systems. With improvements desired with respect to both mechanical properties like strength and toughness as well as more practical properties like weldability, all while lowering the cost, it is important to understand how processing parameters used in the production of these high-strength low-alloy grades affect the structure and therefore performance [1].

To date, the primary factors investigated for improvement in the performance of X70 steels are alloy effect and rolling conditions as these will have the largest effect on the final microstructure of the steel. Studies have looked at the effect of limiting versus increasing niobium content on both the forming of pipes and fracture toughness [1]. In addition, they've also analyzed how the micro-alloy additions such as titanium (*Ti)*, vanadium (*V)*, and niobium (*Nb)* precipitate out as metal carbides, nitrides, or carbo-nitrides during thermo-mechanical processing and the effect of these precipitates on the mechanical properties [2]. For the rolling process, one very important parameter to understand is the continuous cooling behavior of the X70 steel, as this ensures the ideal microstructure can be targeted for the desired application [3]. Studies have also determined the critical temperatures for the rolling process [4]. There is very limited work reported on the effect of the cooling rate during the freezing range for this alloy. Since this grade is typically continuously cast, cooling can be controlled to help obtain a more desirable starting microstructure. One method for the observation of this cooling rate effect on solidification is through the use of the High-Temperature Confocal Scanning Laser Microscope (HT-CSLM).

HT-CSLM has recently begun to increase in prominence as a technique for the direct observation of solidification development as well as other temperature-related microstructural phenomena [5]. This technique is relatively new with the development of confocal microscopy in 1961 by Minski and the addition of infrared heating to allow for high-temperature observation by Emi et al. in the 1990s [6].

The goal of this study is to use the capabilities of the HT-CSLM melting stage to assess the effect of the cooling rate on the behavior of X70 through the freezing range as well as any resultant impact on the remainder of sample cooling.

EXPERIMENTAL PROCEDURE

Production of Material

The material was melted in a 100-lb coreless induction furnace under ultra-high-purity argon cover. High-purity induction iron was used as the base charge material. Ferroalloys were used to introduce silicon, and niobium. Graphite and electrolytic manganese were used to add carbon and manganese to the melt. The melt was deoxidized in the tap stream using pure aluminum shots before the *Fe-Ti* was added and stirred into the 100-lb ladle.

The material was poured into a large dog bone-shaped cylindrical mold constructed of phenolic resin-bonded silica sand (Figure 1). The mold was equipped with copper chills over the two ends of the dog bone and an insulation sleeve over the region where the test material was sectioned from that was also employed to investigate the hot tearing sensitivity of the alloy

as part of a previously published study [7]. In that study a tensile force was applied to the dog bone mold after it had been poured once only the insulation sleeve and the riser had liquid remaining. This tensile force perpendicular to the growth of the dendrites during solidification was used to identify how much force the solidifying shell could withstand before a defect, ideally a hot tear, opened in the insulated region of the casting [7].

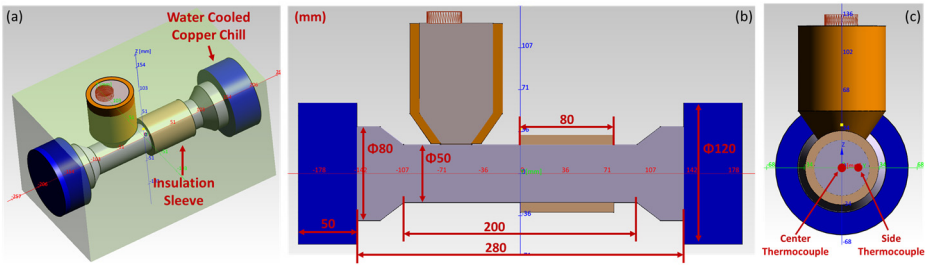

Figure 1. Schematic of the mold that the confocal samples were obtained from showing (a) an overall view of the rounded dogbone shape and the insulated area where samples were sectioned from, (b) a cross section of the mold better showing positioning of the insulation sleeve relative to where the mold is poured, and (c) positioning of the S-type thermocouples within the insulation sleeve which were used to calculate the average cooling rate through the freezing range in the test region [7].

The chemistry of the resulting melt was determined using optical emissions spectrometry (OES) on an immersion puck sampler collected after all additions but before tapping and is reported in Table 1. The carbon and sulfur values were determined using LECO *C-S* combustion analysis conducted according to ASTM Standard E1019 and using samples sectioned from vacuum pins collected from the melt at the same time as the immersion puck [8].

Table 1. Composition of the Test Material With *C* and *S* Obtained Using LECO *C-S* Combustion Analysis and the Remaining Elements Measured by OES

	C*	***Si***	***S****	***Mn***	***Cr***	***Mo***	***Ni***	***Al***	***Nb***	***Ti***
X70	*0.05*	*0.22*	*0.003*	*1.42*	*0.035*	*0.001*	*0.017*	*0.002*	*0.042*	*0.006*

Design of Test

The High-Temperature Confocal Scanning Laser Microscope (HT-CSLM) tests were designed using the data from the thermocouples in the insulated region of the casting mold (Figure 1 (c)) combined with JMatPro equilibrium simulations conducted using the as-cast composition [7, 9].

The test thermocouple data was analyzed using a Fourier transformation in order to convert the as-measured time versus temperature data to fraction solid versus temperature and fraction solid versus time plots (Figure 2) [7]. This allowed the average cooling rate through the freezing range to be identified (26°C/min). Three additional cooling rates were tested to assess the effect of increased cooling rate (50°C/min and 150°C/min) and lowered cooling rate (5°C/min) on the solidification observed during the freezing range. Figure 3 presents the schematic of the test design for this experiment showing the effect of changing the cooling rate through the freezing range on the overall test time. All tests returned to cooling rate of 150°C/min once moved past the freezing range. The reason being tests longer than an hour in length can become impractical to run due to data size and the requirement to focus the laser manually throughout the test. As the freezing range was being studied in this test, cooling rate after solidification was kept constant to avoid additional variables in the remaining phase development once the sample was solidified.

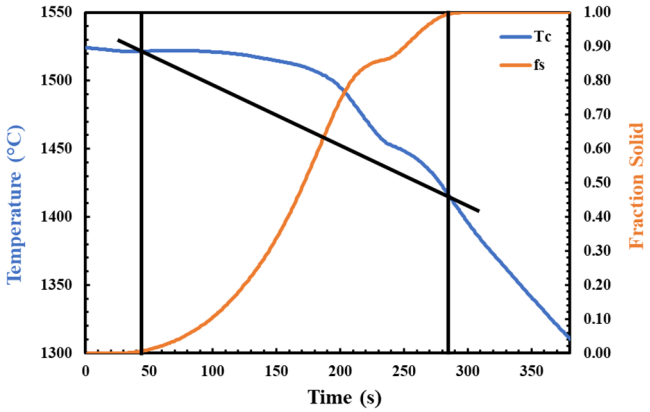

Figure 2. Calculation of the average cooling rate through the freezing range, as shown within the black boundary lines on the cooling curves.

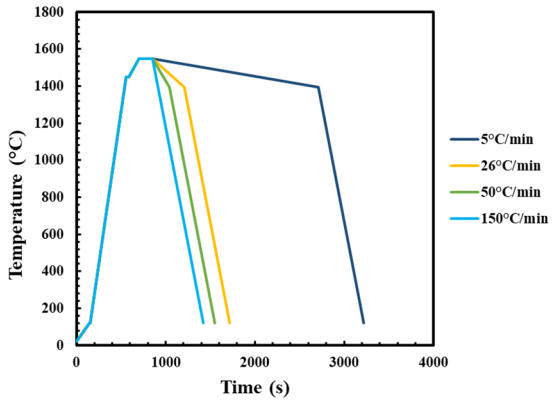

Figure 3. Schematic of test design for this experiment showing the effect of changing the cooling rate through the freezing range on the overall test time. All tests returned to 150°C/min once out of the freezing range.

The temperatures for the liquidus and solidus from both the Fourier transformation and JMatPro were used to ensure optimal temperature selection for the confocal experiments (Table 2) [9]. In total seven tests were conducted, with the first test being used to confirm the proper selection of freezing range and practicality of cooling rate transitions with respect to instrument limitations (Table 3). The first three of these tests were conducted at a cooling rate of 26°C/min through the freezing range and these were followed by two tests cooling through the freezing range at 50°C/min. Upon the completion of these five tests, a single test was conducted using a 5°C/min and a 150°C/min cooling rate through the freezing range. The final test parameters are shown in Table 4. The hold times and ramp temperatures outside of the freezing range were determined based on equipment limitations and past experience. In all cases, step 1 functioned to slowly ramp up the halogen bulb to allow for the optimal lifetime of the filament. The exact parameters of ramping to 120°C at 40°C/min were recommended upon equipment installation. A short hold of 10s was enacted after ramping to 120°C to allow the temperature to begin to equilibrate. From here, a quick ramp to above the liquidus was targeted. However, the higher the ramp rate, the larger the overshoot before stabilizing on the target temperature. 1450°C was targeted first at the higher heating rate of 200°C/min and allowed to stabilize for 30s before heating proceeded to above the liquidus at 50°C/min to ensure that the maximum targeted temperature was close to the maximum achieved temperature. The 120s hold during the preliminary test was extended to 150s during the final testing schedule. This window of time allowed the sample to melt and provided enough time for the optimal solidification observation location to be identified. The final cooling rate of 150°C/min was selected as it is the fastest cooling rate this HT-LSCM can maintain without the use of any alternate cooling source.

Table 2. Liquidus and Solidus Temperatures Predicted Using Both a Fourier Analysis From Experimental Test Data, and an Equilibrium Solidification Simulation in JMatPro [9]

	Liquidus (°C)	**Solidus (°C)**
Fourier	*1522*	*1403*
JMatPro	*1523*	*1491*

Table 3. HT-LSCM Melting Plan for the Preliminary Test With the X70 Samples

Step	Temperature (°C)	Ramp Rate (°C/min)	Hold Time (s)
1	*120*	*40*	*10*
2	*1450*	*200*	*30*
3	*1550*	*50*	*120*
4	*1525*	*-50*	*0*
5	*1395*	*-26*	*0*
6	*80*	*-150*	*10*

Table 4. HT-LSCM Revised Melting Test Plan for the Remainder of the X70 Samples and Cooling Rates

Step	Temperature (°C)	Ramp Rate (°C/min)	Hold Time (s)
1	*120*	*40*	*10*
2	*1450*	*200*	*30*
3	*1550*	*50*	*150*
4	*1395*	*(-5, -26, -50, or -150)*	*0*
5	*80*	*-150*	*10*

Testing of Material

Sample material was machined into 5 mm diameter disks that ranged in weight between 0.35 -0.38 g. The disk was placed into an alumina crucible that had an outer diameter of 6.5 mm and an outer height of 3 mm with a wall thickness of approximately 0.5 mm.

Melting experiments were conducted using a Lasertec VL2000DX-SVF17SP High-Temperature Confocal Scanning Laser Microscope (HT-CSLM), where the heating was provided to the gold-plated chamber using a 1.5 kW halogen bulb and the imaging was conducted using a 405 nm wavelength violet laser. Chamber temperature was measured and controlled using an R-type thermocouple built into the platinum sample stage (Figure 4). Melting was conducted under an ultra-high-purity argon atmosphere. Nominal levels of oxygen in the chamber were ensured through the implementation of multiple vacuum purges prior to the argons' final entry into the system through filters that function as oxygen getters.

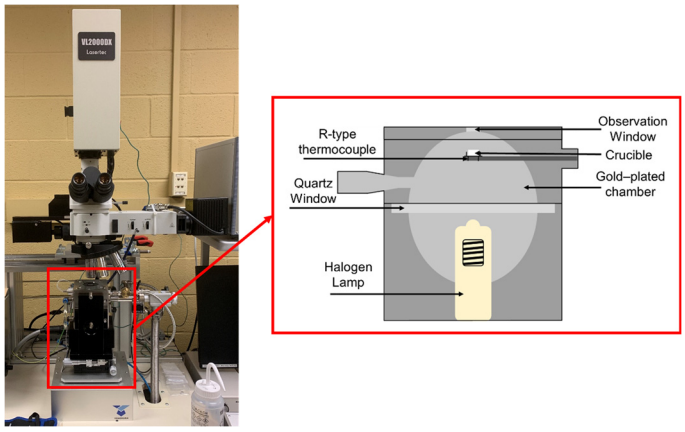

Figure 4. HT-CSLM melting stage and schematic showing the relative positioning of the crucible to the heat source and temperature measurements.

Analysis of Samples

Post-test analysis was conducted on the solidified samples using a TESCAN Scanning Electron Microscope (SEM). Samples were placed on adhesive carbon dots which were adhered to aluminum pin mounts. These pin mounts were attached to the SEM stage so that the non-metallic inclusions and surface features could be analyzed using both back-scattered electrons (BSE) and secondary electrons (SE). Energy dispersive spectroscopy (EDS) was used to identify the approximate chemistry and therefore the likely identity of present non-metallic inclusions.

Phase Prediction

In conjunction with the solidification experiments in the confocal microscope, it was important to know what phases and precipitates were expected during the solidification. Commercial software JMatPro was used to conduct equilibrium simulations, and FactSage was used to conduct both Scheil and equilibrium simulations [9,10]. The JMatPro equilibrium and FactSage Scheil simulations were conducted with the base composition to predict the phase formation in the major portion of the matrix material (Figure 5). However, since the steel is completely melted in the confocal before resolidification, it behaves like as-cast material, and the last liquid to solidify will become solute enriched and generate a higher concentration of inclusions late in the solidification process. To account for this, the composition of the last fifteen percent of liquid from the Scheil simulation was used in equilibrium simulations in both FactSage and JMatPro to more accurately assess the differences in phases and temperature of transformations for the solute enriched areas. This simulation was conducted twice using compositions with one difference, the carbon content (Table 5). In a practical assessment of the segregated regions in steel, the carbon enrichment in the interdendritic regions is often less than that predicted by the Scheil model due to the high mobility of the carbon. Because of this, the enriched liquid composition was assessed with both the equilibrium carbon content (Figure 6) as well as the determined enriched value (Figure 7) to get a broader assessment of possible phase formation during solidification. A summary of the predicted phases and the temperatures they are present at for each simulation is contained in Table 6. In all simulations, the same five components are seen with varying start times and amounts of each phase: austenite, ferrite, cementite, *NbC*, and *MnS*. The JMatPro simulation with the base composition as well as the last 15 percent liquid composition with the base carbon level both show the appearance and dissolution of $Ti_4C_2S_2$. In addition, in all simulations except for the Scheil prediction, both delta ferrite and alpha ferrite are predicted to be present during the solidification process. It is also apparent that increased levels of the *NbC* and *MnS* should be expected, regardless of carbon content, in the last regions to solidify. It should also be noted that oxides and nitrides will form in this steel, however, since *O* and *N* contents are unknown, they've been excluded from the prediction simulation.

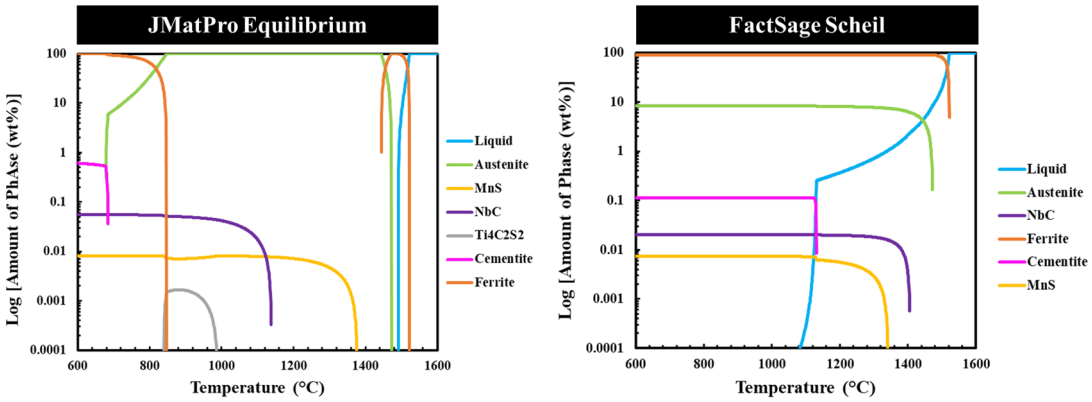

(a) (b)

Figure 5. Predicted (a) equilibrium and (b) Scheil solidification of the X70 alloy tested, using the base composition.

Table 5. Composition of the Last 15% Liquid Predicted by the Scheil Solidification Simulation

	C*	***Si***	***S****	***Mn***	***Cr***	***Mo***	***Ni***	***Al***	***Nb***	***Ti***
Scheil Carbon	*0.26*	*0.47*	*0.018*	*2.24*	*0.042*	*0002*	*0.024*	*0.001*	*0.16*	*0.022*
Original Carbon	*0.05*	*0.47*	*0.018*	*2.24*	*0.042*	*0002*	*0.024*	*0.001*	*0.16*	*0.022*

Note: Two compositions were selected as the carbon diffusion is typically overpredicted by Scheil.

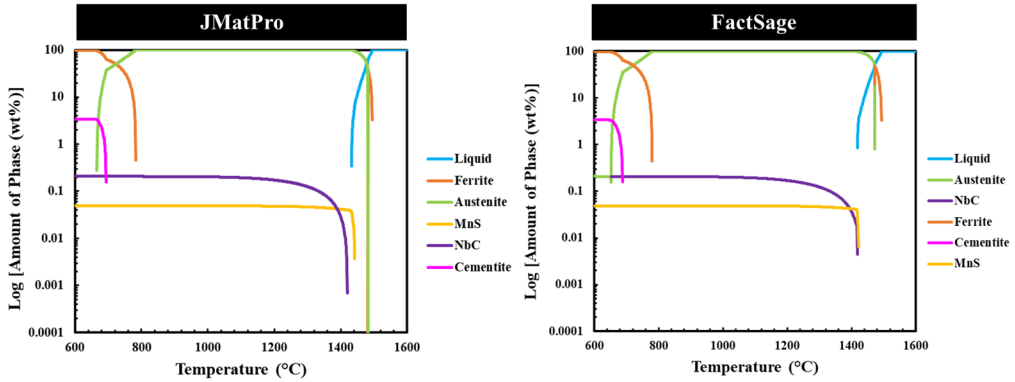

(a) (b)

Figure 6. Equilibrium solidification of the last 15% liquid as calculated using Scheil simulation and assuming the fully predicted diffusion of carbon is achieved as calculated using (a) JMatPro and (b) FactSage.

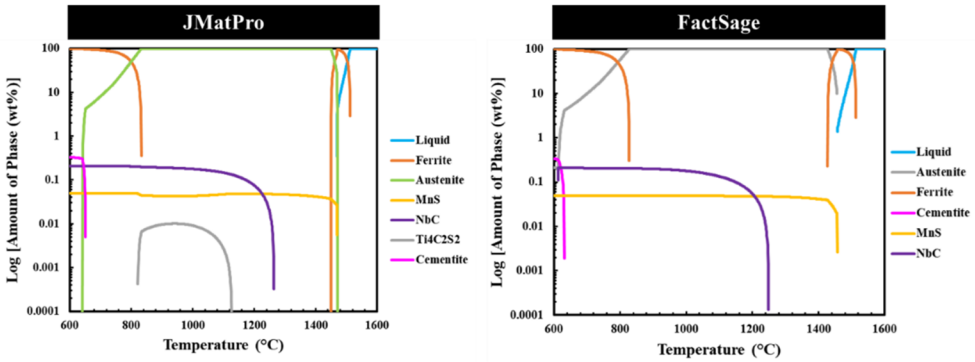

(a) (b)

Figure 7. Equilibrium solidification of the last 15% liquid as calculated using Scheil simulation and assuming the carbon content doesn't change from the base levels.

Table 6. Predicted Transformation Temperatures as Achieved in Scheil and Equilibrium Calculation Using Both the Base and Last 15 wt.% Liquid Calculation From the Scheil Simulation

		Base Composition		**Last 15 Percent Liquid Composition**			
				Scheil Calculated C		***Base Alloy C***	
		JMatPro Eq.	**FactSage Scheil**	**JMatPro Eq.**	**FactSage Eq.**	**JMatPro Eq.**	**FactSage Eq.**
Liquid Behavior	Liquidus	1523	1522	1496	1494	1512	1513
	Solidus	1491	1112	1432	1418	1469	1457
Delta Ferrite	Start	1491	1522	1432	1418	1469	1457
	Finish	1444		1481	1472	1449	1427
Austenite	Start	1473	1472	1482	1473	1471	1456
	Finish	678		656	652	641	613
Alpha Ferrite	Start	847		783	780	833	828
Cementite	Start	684	1131	694	688	652	632
MnS	Start	1377	1341	1443	1422	1470	1457
NbC	Precipitate	1138	1405	1420	1418	1264	1249
	Dissolve				652		613
$Ti_4C_2S_2$	Precipitate	989				1128	
	Dissolve	839				821	

RESULTS AND DISCUSSION

HT-LSCM Solidification

All tests closely followed the planned temperature profile, with little deviation until the sample cooled to around 200°C. For each cooling rate, with the exception of 26°C/min, the initiation of solidification was only observed for one sample. However, in the preliminary test, 26°C/min sample A, the solidification started before the cooling rate was shifted from 50°C/min to 26°C/min. Therefore, 26°C/min sample C, 50°C/min sample B, the 150°C/min sample, and the 5°C/min sample were selected for characterization as representative of their respective cooling rates.

Table 7 contains the transformation temperatures, depicted graphically in Figure 8, for all seven samples tested. As future work is pursued using X70, or other similar alloys, the difference between the predicted and measured temperatures can be used to develop a correction factor. This will help better account for the difference between the temperature the sample is experiencing in the field of view and the temperature at the bottom of the crucible where the thermocouple is positioned. As expected, all samples had near identical liquidus temperatures (1548-1551°C). However, while all similar they were all at least 25°C above the closest prediction (JMatPro base composition equilibrium) . Transformation 1 upon heating and transformation 2 upon cooling are transformations between the same two phases. During these transformations, migration of the grain boundaries was observed and due to measured temperatures in lower to mid-1400°C range this would be the transition to delta ferrite from austenite upon heating and from delta ferrite to austenite upon solidification. Based upon the solidification predictions, transformation 1 was expected to occur at a higher temperature. However, it must be considered that the temperature being measured is from the bottom of the crucible while the top of the sample under observation would likely be hotter, especially considering the high heating rate used at the beginning of the experiment. Upon cooling, the average temperature that transformation 2 occurred at (1416°C) was once again lower than expected. Austenite should start forming in the mid to high 1400°C range. There are a few possible explanations for this. Firstly, it is possible that upon heating there was a temperature difference between the surface where the transformation was observed and the stage where the temperature was measured. In addition, and perhaps more likely, a high magnification is required for the observation of these transformations that resulted in a limited field of view. It is possible that while some areas of the sample started transforming closer to the predicted temperature, the area in view was partly or even mostly transformed already.

Table 7. Transformation Temperatures as Measured From the HT-CSLM for the Tested Samples

	26°C/min			**50°C/min**		**150°C/min**	**5°C/min**	**Average**	**Standard Deviation**
	A	***B***	***C***	***A***	***B***				
Transformation 1	1429	1431	1427	1419	1440	1439	1440	1432	7
S→L Start	1506	1512	1528	1538	1511	1506	1549	1521	16
All L	1549	1548	1551	1548	1549	1550	1550	1549	1
L→S start	1531	-	1518	-	1502	1473	1535	1512	22
Transformation 2	1413	1414	1403	1413	1426	-	1425	1416	8
Inclusion /Precipitation	1181	1116	1145	1152	1163	1087	1079	1132	36
Transformation 3	718	762	724	714	700	686	807	730	38

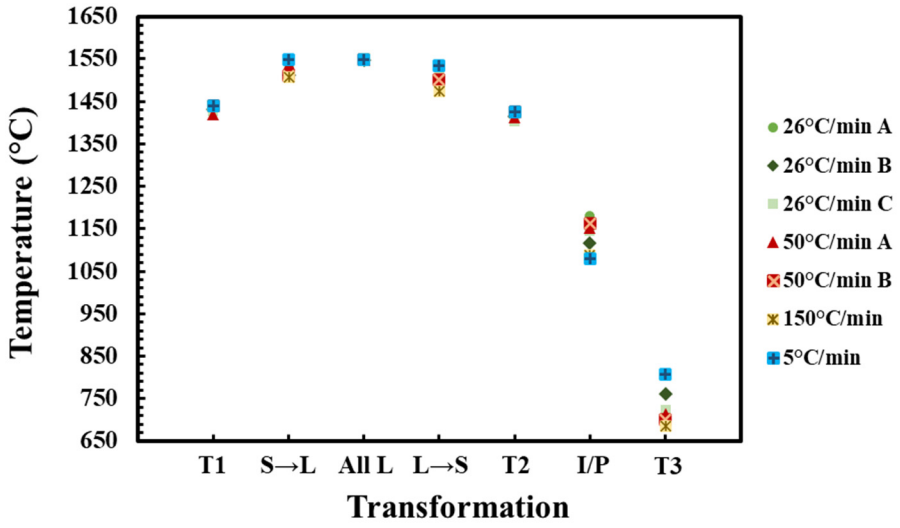

Figure 8. Transformation temperatures as measured from the HT-CSLM for the tested samples.

The inclusions observed precipitating from the matrix are likely the *NbC*, the $Ti_4C_2S_2$, or both species based upon the phase predictions (Figure 9). They typically precipitated between 1100°C and 1200°C which is too low to be the *MnS*. This is lower than most of the predictions for the formation of the *NbC* with the exception of the JMatPro base composition equilibrium [9]. However, it is very similar to the temperature range predicted for the Titanium carbo-sulfides. The $Ti_4C_2S_2$ is predicted to dissolve back into the matrix, so it is likely that the precipitates seen are the *NbC* as they remain present through transformation 3 (Figure 10).

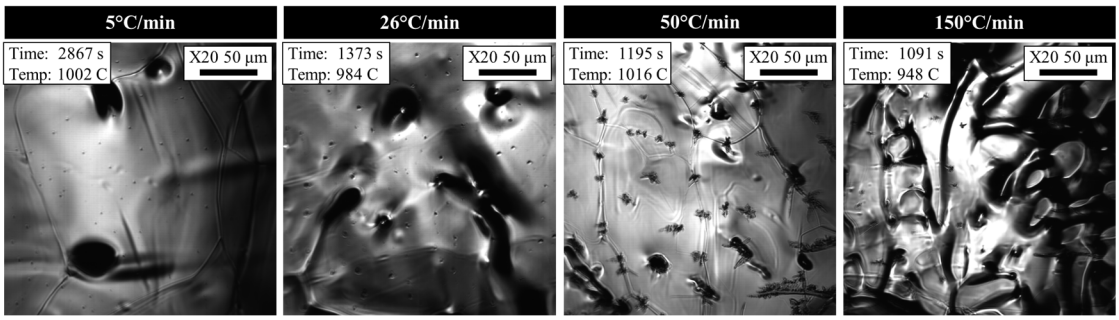

(a) (b) (c) (d)

Figure 9. Similar precipitation was observed for all four samples, (a) 5°C/min, (b) 26°C/min, (c) 50°C/min, and (d) 150°C/min, at varying initiation temperatures. However, the precipitates formed for the 50°C/min sample B are larger and more complex than the other samples.

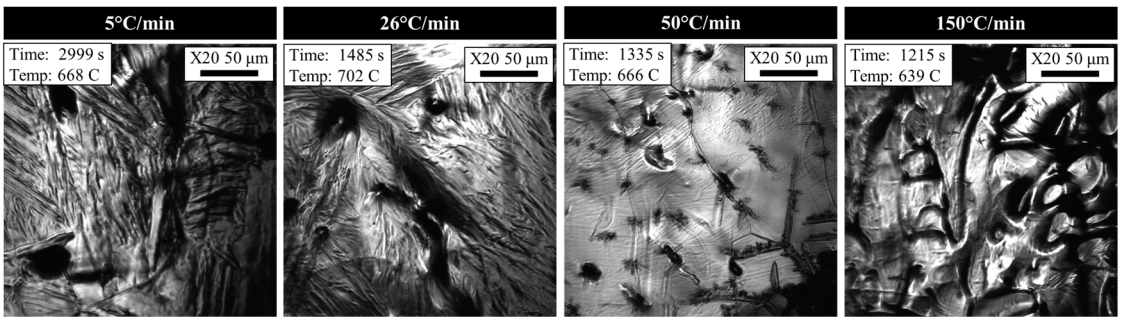

(a) (b) (c) (d)

Figure 10. Similar solid state phase transformations were observed for all four cooling rates: (a) 5°C/min, (b) 26°C/min, (c) 50°C/min, (d) 150°C/min. 26°C/min sample C and 50°C/min sample B were chosen as representatives for their cooling rates. However, the slower cooling rates seemed to have thicker and more pronounced lath structures.

Transformation 3 occurred at an average temperature of 730°C/min. It is interesting to note that the samples that had a slower cooling rate through the freezing range seemed to experience transformation 3 at a higher temperature despite all the samples cooling through this region at the same rate (150°C/min). These faster cooling rate samples (150°C/min and 50°C/min) seem to have developed a finer structure during this transformation than the slower rates (5°C/min and 26°C/min) which experienced the growth of a thicker, more pronounced plate like structure (Figure 10 (a) and (b)). Based on the temperature predictions, this was the transformation to alpha ferrite from austenite. Mu et al. conducted a review of experiments that used the HT-CSLM to study ferrite formation [5]. They primarily assessed papers with steels designed to have certain inclusions rich in *Ti*, *Si*, *Al*, *B*, and *Mg* as well as *MnS*. In particular, they highlighted example images of grain boundary ferrite (GBF) and inter-granular ferrite (IGF) formation in a TiO_2 containing steel as observed in the HT-CSLM. The lath like structures observed in that study look similar to those observed for the 5°C/min and 26°C/min samples [5]. This would also be expected as the 26°C/min sample should be replicating the as-cast condition, which was primarily ferritic with some pearlite colonies present (Figure 11). It still needs to be considered that all of the samples went through the transformation at 150°C/min (2.5°C/s). The maximum cooling rate achieved during the solidification of the test mold was 1.34°C/s (80°C/min) as shown in Figure 12. However, the average cooling rate near 730°C where the transformation occurred was 0.12°C/s (7°C/min). Based on the continuous cooling transformation (CCT) curves calculated in JMatPro for this alloy composition (Figure 13) all three of these cooling rates should fall within regions with the same phases present, just in different proportions. This would indicate the presence of ferrite and pearlite as well as bainite. The transformation observed in the HT-CSLM tests occurred after passing through the ferrite nose but before entering the bainite nose. This would agree with the assessment that the phase transformation is austenite to alpha ferrite. Yang used a Gleeble-3500 to construct an experimental CCT diagram for a similar X70 steel with a higher *Mo* (0.17wt%) and *Al* (0.041wt%) content than this experiment [3]. They found that for a static test with no deformation, for a cooling rate close to 1°C/s, a microstructure of primarily polygonal ferrite with a small amount of pearlite, as observed in the as-cast sample, should be present. This carries forth as the cooling rate continues to get smaller. As the cooling rate increases the structure becomes completely acicular ferrite at 5°C/s, and transitions to polygonal ferrite in the region between this point and 1°C/s [3]. Therefore, cooling through this region at 2.5°C/s (150°C/min) could lead to the presence of a small amount of acicular ferrite. Lee et. al. studied acicular ferrite transformations in the HT-CSLM for a high strength low alloy (HSLA) steel. The acicular ferrite present looked like thick black lines, scattered throughout the matrix [11]. While it is difficult to confirm, some of these thicker crack-like features indicating that acicular ferrite is present have formed in the 50 and 150 °C/min cooling rate samples (Figure 10 (c) and (d)).

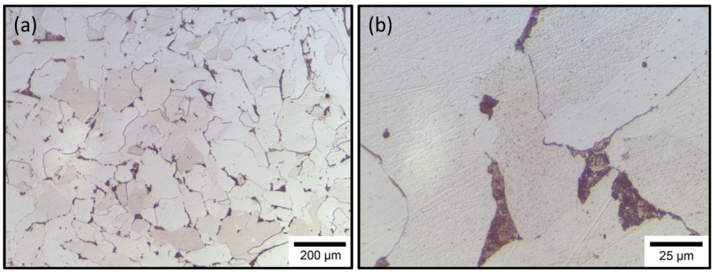

Figure 11. As cast microstructure of X70 steel was sectioned out of the same region as the confocal samples and etched with 2% Nital. Micrographs show the primarily ferritic microstructure (a) low magnification with the presence of some pearlitic colonies (b) higher magnification.

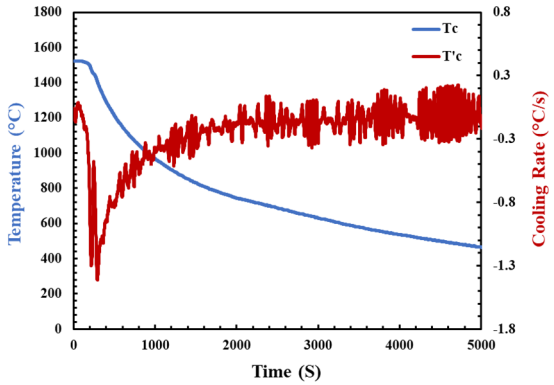

Figure 12. Changes in the cooling rate in the casting that the samples were sectioned from as the sample solidified and cooled.

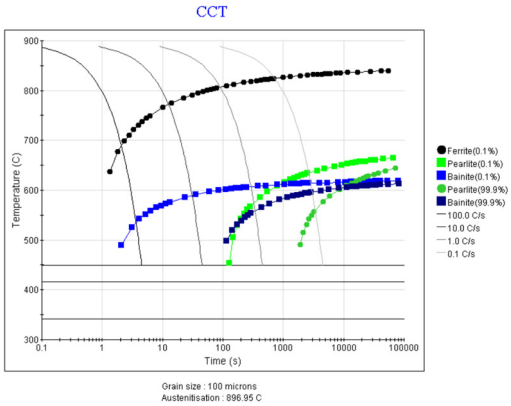

Figure 13. Calculated CCT diagram using the base alloy composition in JMatPro [9].

The start of solidification followed the same temperature trend observed during the transition to ferrite (transformation 3). The slower the cooling rate, the higher the temperature at which solidification was observed. In addition, the average temperature at which this transformation occurred, 1512°C, is very similar to the temperature range predicted for the liquidus for this alloy. When cooled down just below the liquidus solid is expected to begin forming. The HT-CSLM technique is limited by its ability to resolve large focal depths. As the sample wets to the crucible and forms a meniscus or develops high levels of surface texture during the solidification, it can become harder to obtain optimal focus [6]. This made it difficult to determine the solidus point and therefore the overall changes in the solidification window with the change in cooling rate through the freezing range. However, there are clear changes in solidification morphology as the cooling rates change.

At 5°C/min, the solidification is very directional and the solidification progressed across the view in one front. The solidified surface was smooth with very few surface features (Figure 14). In this case, the smooth boundary between the liquid front and the solid indicated a mostly stable planar solidification [12]. The morphology combined with the slow velocity of the solidification front compared to the other samples would indicate that the solidification progressed at a rate below the critical velocity for the perturbation of a cellular structure [13].

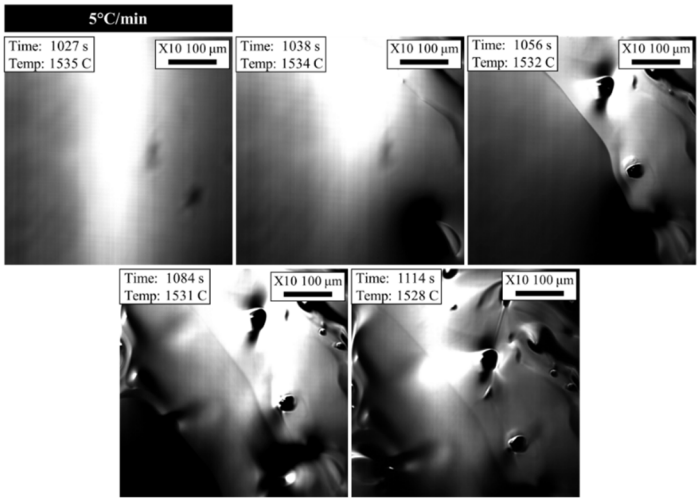

Figure 14. Solidification of X70 cooled at 5°C/min through the freezing range. The sample experiences smooth, possibly planar, directional growth.

When the cooling rate was increased to 26°C/min the solidification first developed as small protrusions from the melt. After a slower initial growth, the rate of the appearance of the solidified structure increased and within the field of view, two solidification fronts developed concurrently moving towards the center of the frame (Figure 15). In this case, due to the uneven spacing and arrangement of the protrusions from the melt, these would be cellular islands forming prior to the planar solidification front. At this cooling rate, the solidification front has become less stable and was bordering between cellular and planar solidification [12].

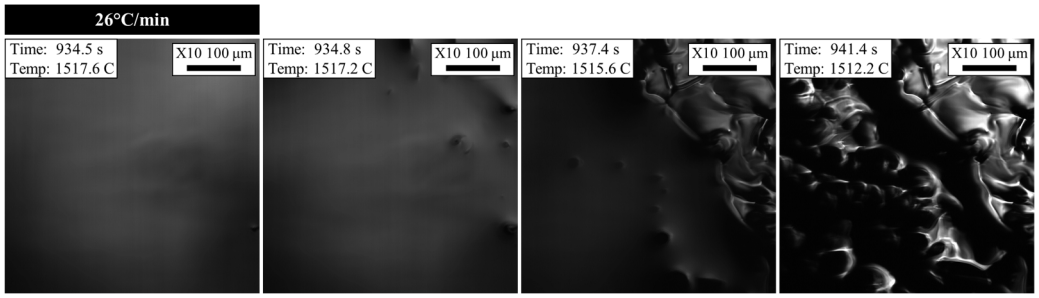

Figure 15. Solidification development of X70 sample C cooled at 26°C/min through the freezing range. The sample experiences dendritic solidification directionally across the plane of view.

With the increase of the cooling rate to 50°C/min the solidification started as localized islands. As the sample continued to cool, the solidification front grew in from all sides towards the center of the image and the original solidified islands. There also appeared to be a darker region that based on morphology was expected to be an inclusion-rich region (Figure 16). These islands formed first appeared to be islands of delta ferrite forming prior to the solidification front [6]. The primary solidification front that moved in with the front containing the inclusions had less surface texture than that found for the 26°C/min sample. It also had a much higher inclusion presence than the other samples. It is possible that this sample was sectioned closer to the centerline of the casting and therefore contained a slightly enriched composition compared to the material of the other samples [14]. The critical velocity to cause the transition from planar to cellular solidification could have shifted with the altered composition, leading to a smoother solidification than observed in the 26°C/min sample, but still a solidification that contained some cellular growth [13].

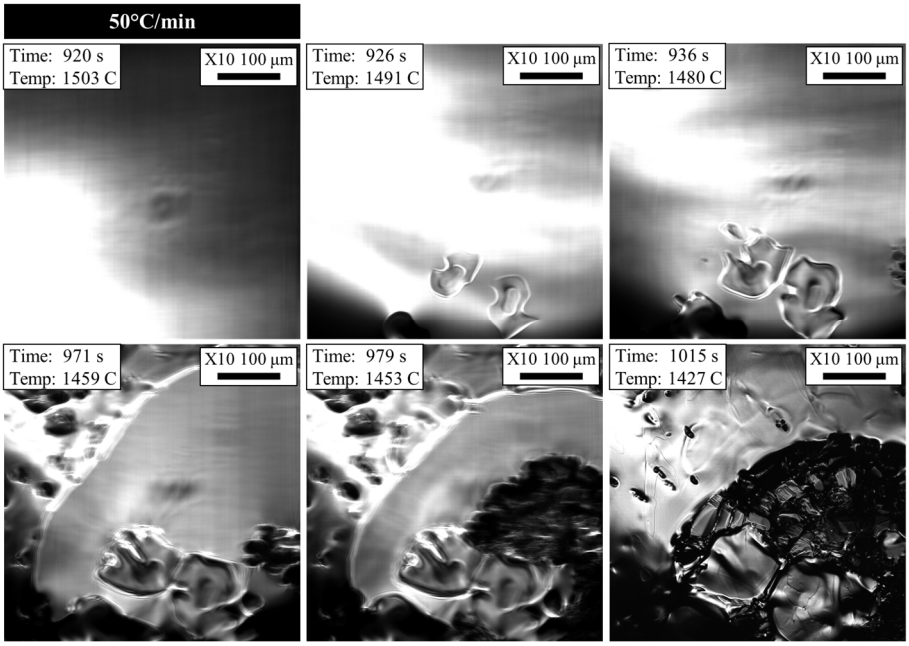

Figure 16. Solidification development of X70 sample B cooled at 50°C/min through the freezing range. The sample experiences a mixture of local cellular growth, with the rest of the field of view solidifying towards the center of the image and the initial cellular regions.

Once the cooling rate increased to 150°C/min through the freezing range, the solidification once again became a sweeping directional front like in the 5°C/s sample. However, in this case, the solidification progressed much faster, and rather than the formation of a smooth solidified surface, the morphology appeared as a network with a high level of topography (Figure 17). This solidification is harder to classify. It must be considered that when assessing larger samples, the field of view is the top of the crucible and that the top and bottom of the crucible will be the hottest points with a larger gradient towards the central portion of the sample. This means that the bulk solidification will not be represented in the surface being viewed. In addition, the direction of solidification appeared in the frame of view to be growing from the edge of the crucible towards the center but it could also have been growing from the bottom of the crucible to the top and this is difficult to confirm [12]. A method called concentric solidification has been proposed by Reid et al. to address this issue, however, it requires samples of a thickness less

than 250 µm which can be difficult to produce. Samples of 250 µm also do not have enough material to section and observe the through thickness microstructure like larger samples would [6]. Even the 2.5 mm tall samples used in this study proved difficult to section and obtain information about the solidification direction. While the smooth motion of this solidification appeared planar, the solidified microstructure looked similar to a cellular or dendritic structure. Although, with the direction of solidification, no dendrites could be observed during the test or on the sample surface when examined in the SEM. This would indicate that, like the previous samples, solidification was somewhere between the planar to cellular transition, and in this case, was closer to cellular growth.

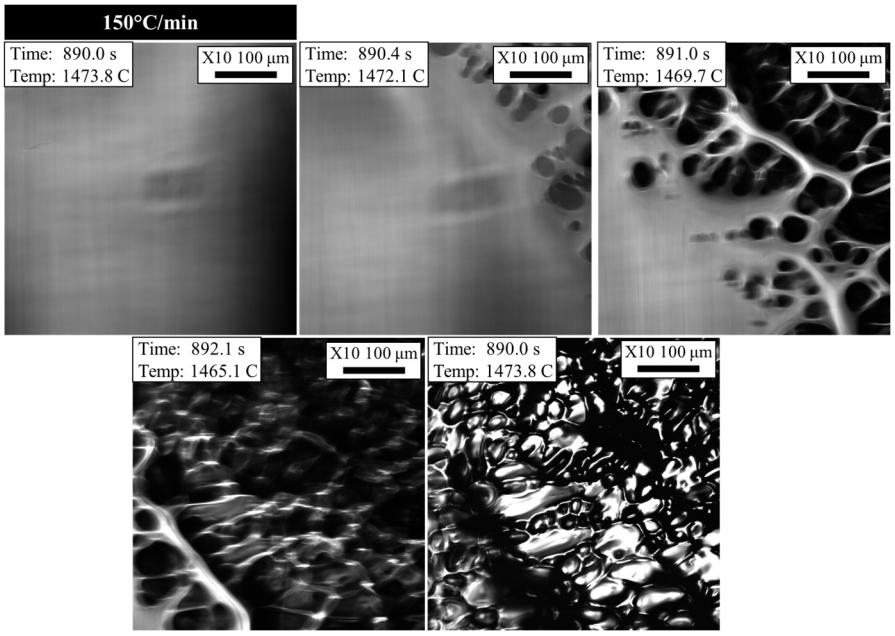

Figure 17. Solidification development of X70 cooled at 150°C/min through the freezing range. This sample solidifies with the highest degree of surface topography and the smallest surface features. Solidification appears planar, but due to different possible directions of solidification, it is difficult to confirm.

SEM Analysis of Solidified Samples

Four out of the seven samples were analyzed in the SEM: the 26°C/min sample C, 50°C/min sample B, the 150°C/min sample, and the 5°C/min sample. BSE analysis was used to identify the nonmetallic inclusions and their distribution across the surface of the melted sample, and SE mode was used to assess the topography of the sample (Figure 18). Similar to what was observed in the HT-CSLM during the melting, the 5°C/min sample had very little surface topography, and other than the onset of a small crater, it was free of any larger solidification shrinkage or other defects. The three other samples all had large craters developed across the surface that contained a smaller secondary crater towards the bottom-center of the larger crater. These were attributed to solidification shrinkage as the smaller crater contained a large cluster of inclusions (Figure 19) [14]. In the case of the slowest cooling rate (5°C/min) only *Al* rich inclusions were observed. Due to the curved surfaces, the EDS results were not as accurate as they are for polished samples. Therefore, the as-cast microstructure was also analyzed for comparison (Figure 20). The *Al-rich* inclusions in the as-cast microstructure were primarily alumina and titanium-rich alumina. Despite the fact that little to no oxygen was measured for these inclusions, these inclusions in the crater can likely also be classified as *Ti-rich* alumina (Figure 21). While it's hard to confirm, compared to alumina on the curved sample surface, these are likely similar to what Dorrer et al. termed AT(a) inclusions. These typically have lower titanium contents ranging from 0.35 to 7 wt.%. With this low *Ti* level, they are nearly identical in morphology to traditional alumina inclusions. Their study found that most of the *Al* and *Ti* containing inclusions they identified in their samples fell within this AT(a) category [15].

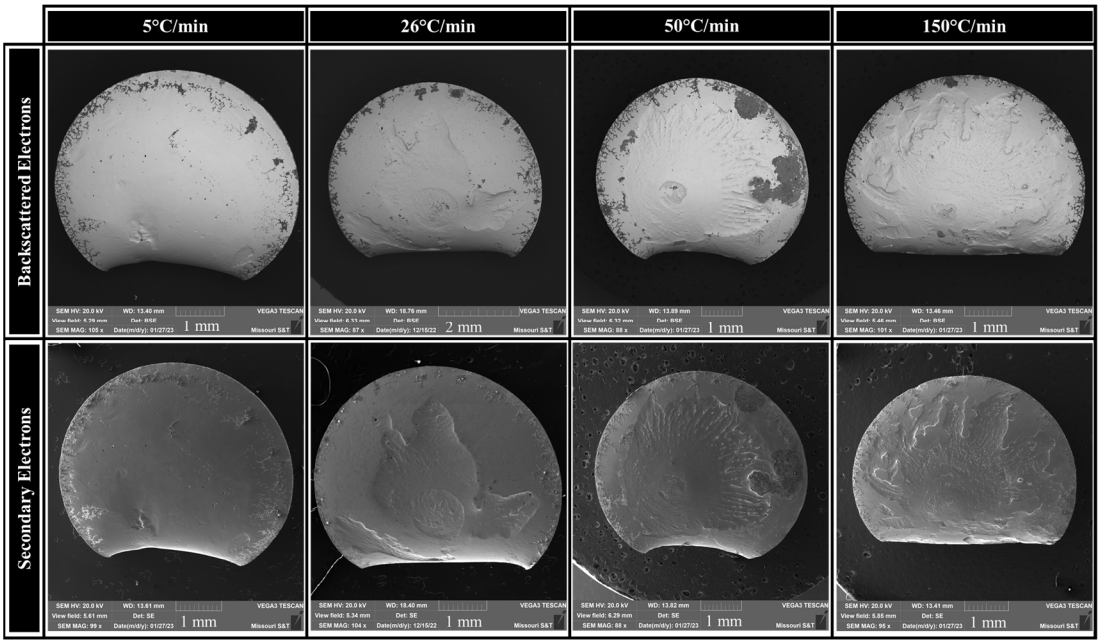

Figure 18. BSE and SE images of sample surfaces showing larger solidification shrinkage craters as the cooling rate becomes faster. 26°C/min sample C and 50°C/min sample B were chosen as representatives for their cooling rates.

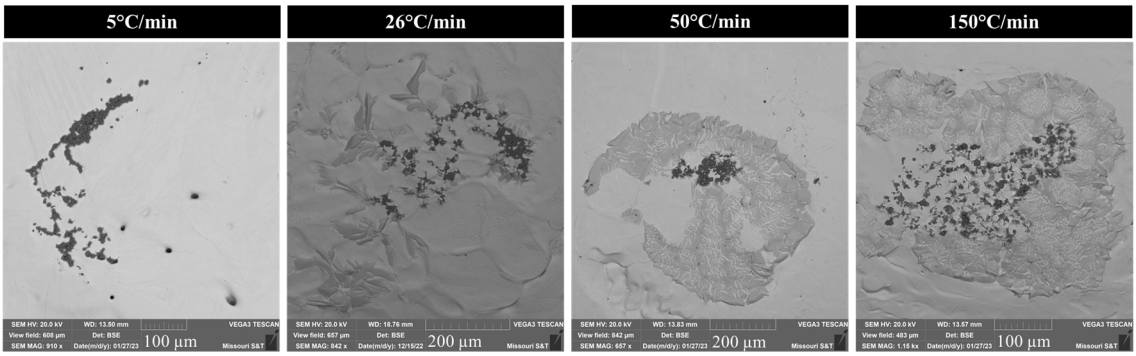

(a) (b) (c) (d)

Figure 19. BSE images show increasing size and complexity of inclusion presence in the solidification shrinkage craters for (a) 5°C/min cooling rate, (b) 26°C/min sample C, 50°C/min sample B, and (d) 150°C/min.

	Wt%
C	1.4
O	10.7
Al	50.6
Fe	37.3

	Wt%
C	1.7
O	18.8
Al	54.4
Ti	13.5
Fe	11.6

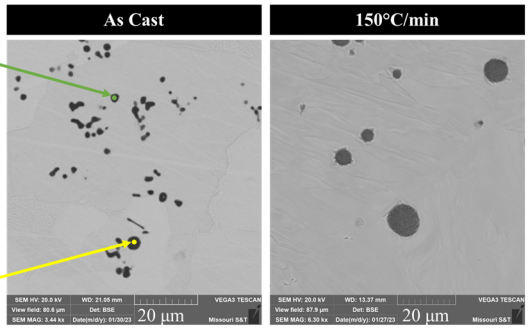

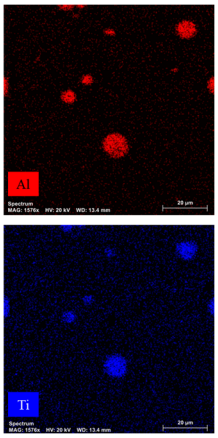

Figure 20. BSE images of inclusions seen on the surface of the 150°C/min sample as compared to inclusions found on the as cast condition of the casting that test material was sectioned from.

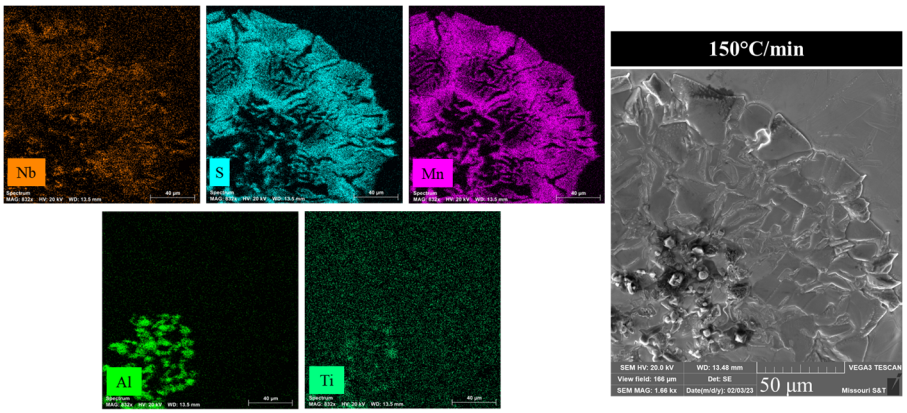

Figure 21. SE image showing example of the topography of the inclusion rich region in the solidification shrinkage crater for the 150°C/min sample. The outer, more geometric, polygonal structure appears to be *Nb* rich *MnS*. The inner structure appears to be *Al* rich inclusions with some *Ti* presence.

In the 26°C/min sample some small regions of *MnS* started to form around the central alumina inclusions in the center of the smaller crater (Figures 19 and 21). Oikawa et al. studied the possible morphologies of *MnS* in steels and when they are likely to occur. Based on the morphologies described in their work, these were classified as angular irregular eutectic *MnS*. This study only covered additions of *C*, *Si*, *Al*, and *Ti* and therefore predicted rod-like eutectic structures. However, X70 has a much higher alloying content than the steels tested by Oikawa et al., and they found this increase made the eutectic structure more prevalent than the other morphologies they observed [16]. The 26°C/min sample was also unique due to the presence of a network of inclusions as shown in Figure 22. This network seemed to be primarily *MnS*, however, there were *Nb* rich particles within the matrix that could be the *NbC*. In this case, the *MnS* appeared closer to rod-like eutectic instead of an irregular eutectic. This could be because this feature is outside of the small crater where the larger networks of *MnS* are contained, which were likely the last area to solidify and therefore likely solute enriched compared to the matrix composition. Therefore, it is possible that the morphology of the *MnS* had enough compositional differences to lead to a different morphology [16].

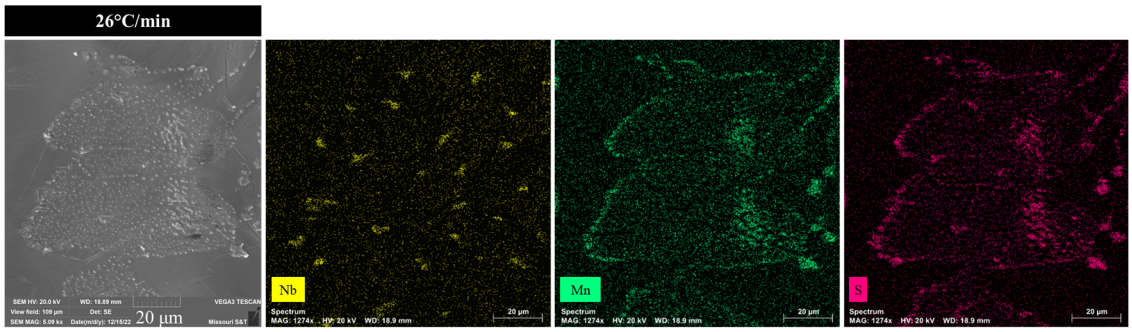

Figure 22. SE image showing a network of inclusions observed on the surface of the 26°C/min sample *C* that appears to be primarily *MnS*, but also seems to contain *Nb* rich inclusions.

The 50°C/min sample had a much higher level of inclusions than the other cooling rates. As previously mentioned, it is likely that this sample was sectioned from close to the centerline of the parent casting and is from a locally alloy-enriched region. Alternatively, the solidification morphology could have led to higher levels of segregation. Overall, the crater of shrinkage in the 50°C/min sample was similar in size to the 150°C/min sample, but there seemed to be larger variations in surface texture in the 150°C/min sample. In addition, the cluster of *MnS* and alumina in the center of the smaller crater were a similar size in both the 50°C/min and 150°C/min samples. This sample was unique in that the 150°C/s cooling rate sample is the only sample where some large circular inclusions could be observed on the surface (Figure 20). Like the as-cast microstructure, these were rich in *Al* and *Ti* and were likely *Ti-rich* alumina inclusions. These inclusions were more accurately categorized as *Al* + *Ti* oxide. They commonly form when *Ti* additions are made after a melt has been deoxidized using aluminum. While these inclusions have a similar BSE contrast to alumina inclusions, they can be distinguished through EDS analysis as well as their spherical morphology as compared to the more irregular morphology of the alumina inclusions [17].

CONCLUSIONS

Samples from an as-cast X70 steel were melted in the HT-LSCM under four different cooling rates (5°C/min, 26°C/min, 50°C/min, and 150°C/min) through the freezing range to assess the effect on the overall alloy solidification. Results were compared to temperature predictions for phase transformations, and the final solidified structures were analyzed in the SEM to assess inclusion presence and morphology.

- Simulations predicted six phases, of which four were observed and maintained a fairly good agreement with the predicted temperature ranges. The samples solidified from liquid as delta ferrite, transitioning to austenite, and then to alpha ferrite. While *NbC* were predicted and observed during the melting trials, they were not found on the surfaces of the solidified samples. In contrast, while *MnS* were predicted and not observed in the videos, they were seen in the solidified samples.
- The sample solidified through the freezing range at 5°C/s experienced planar solidification and had a limited inclusion presence on the smooth surface other than *Al-Ti-O* inclusions that resembled the morphology of traditional alumina inclusions.
- Upon an increased cooling rate through the freezing range of 26°C/min some cellular growth was observed in front of the higher surface texture planar solidification front. This sample developed solidification shrinkage on the surface, at the center of the sample where *Al-Ti-O* inclusions as well as angular irregular eutectic *MnS* inclusions formed. The sample also contained an inclusion network that appeared to be eutectic *MnS* with interspersed *Nb* rich particles.
- At a cooling rate of 50°C/min through the freezing range, islands of delta ferrite formed before the planar solidification front moved in. This sample was highly enriched in the angular irregular eutectic *MnS* as well as *Al-Ti-O* inclusions. It also contained a large solidification crater on the sample surface.
- At the highest cooling rate of 150°C/min through the freezing range, the solidification mechanisms were hard to identify but appeared close to the planar to cellular transition. The solidified sample had solidification shrinkage similar to the two lower cooling rates examined, as well as the same *MnS* and *Al-Ti-O* inclusions. However, the highest cooling rate sample also had *Al + Ti* oxide inclusions which had a higher level of *Ti* than the *Al-Ti-O* inclusions and appeared more spherical than globular like traditional alumina inclusions.

In order to better understand the solidification of X70 under these cooling rates additional analysis of the through-thickness direction would be required. Additionally, a concentric solidification technique would need to be developed for this alloy to provide improved control of the solidification conditions such as temperature gradient and cooling rate.

ACKNOWLEDGMENTS

The authors thank undergraduate research assistant Evan Barth for his help with sample preparation. This project was supported by the Peaslee Steel Manufacturing Research Center (PSMRC) at Missouri University of Science and Technology (Missouri S&T). Special thanks to all of the faculty as well as the industrial mentoring committee of the PSMRC for their help and guidance. This project was also made possible due to equipment purchased thanks to Cooperative Agreement Project: W911NF-20-2-0251 with the U.S. Army Combat Capabilities Development Command, Army Research Laboratory, and the Ground Vehicle Systems Center.

REFERENCES

1. F. F. Conde, F.J. Pina, J.M. Giarola, G.S. Pereira, J.C. Francisco, J.A. Avila, W.W. Bose Filho, “Microstructure and Mechanical Properties of Nb-API X70 Low Carbon Steel,” *Metallography, Microstructure, and Analysis,* Vol. 10, August 2021, pp. 430-440.
2. Chen Gu, Michael J. Gaudet, Jing Su, Brian Langelier, Hui Yuan, Nabil Bassim, Hatem Zurob, “Advanced Characterization of Precipitation and Microstructure Heterogeneity in X70 Steel,” *Metallurgical and Materials Transactions A*, Vol. 54, December 2022, pp. 768-775.
3. Hongmei Yang, “Continuous cooling transformation behavior of X70 pipeline steel,” *Advanced Materials Research*, Vol. 690-693, May 2013, pp. 2205-2209.
4. A. Al Shahrani, T. Schambron, A. Dehghan-Manshadi, J. Williams, E. Pereloma, “Effects of Processing Parameters on Microstructure Development in X70 Pipeline Steel,” *Materials Science Forum*, Vol. 654-656, June 2010, pp. 298-301.
5. Wangzhong Mu, Peter Hedstrom, Hiroyuki Shibata, Par G. Jonsson, Keiji Nakajima, “High-Temperature Confocal Laser Scanning Microscopy Studies of Ferrite Formation in Inclusion-Engineered Steels: A Review,” *JOM*, Vol. 70, No. 10, May 2018, pp. 2283-2295.

6. Mark Reid, Dominic Phelan, and Rian Dippenaar, “Concentric Solidification for High Temperature Laser Scanning Confocal Microscopy,” *ISIJ International*, Vol. 44, No. 3, 2004, pp. 565-572.

7. Katelyn Kiser, Simon Lekakh, Mario Buchely, Viraj A. Athavale, Soumava Chakraborty, Ronald J. O’Malley, Laura Bartlett, Krista Limmer, Katherine Sebeck, Daniel Field, “Evaluating the Onset of Hot Tearing in High-Strength and Lightweight Steels Using Controlled Deformation Testing,” *AIST Transactions*, Vol. 20, No. 3, March 2023, pp. 214-226.

8. ASTM Standard E1019, 2018, “Standard Test Methods for Determination of Carbon, Sulfur, Nitrogen, and Oxygen in Steel, Iron, Nickel, and Cobalt Alloys by Various Combustion and Inert Gas Fusion Techniques”, ASTM International, West Conshohocken, PA, 2018, DOI: 10.1520/E1019-18, www.astm.org.

9. JMatPro v. 13.0, Sente Software Ltd., Surrey Technology Centre, Surrey GU 7YG, United Kingdom.

10. C.W. Bale, E. Belisle, P. Chartrand, S.A. Decterov, G. Eriksson, A.E. Gheribi, K. Hack, I.H. Jung, Y.B. Kang, J. Melancon, A.D. Pelton, S. Petersen, C. Robelin, J, Sangster, P. Spencer, M.A. Van Ende, “FactSage v8.1 Thermochemical Software and Databases – 2010-2016,” *Calphad*, Vol. 54, 2016, pp. 35-53.

11. Sang-In Lee, Seung-Hyeok Shin, Hyeonwoo Park, Hansoo Kim, Joonho Lee, Byoungchul Hwang, “In-Situ Observation of Acicular Ferrite Transformation in High-Strength Low-Alloy Steel Using Confocal Laser Scanning Microscopy,” *Archive of Metallurgy and Materials*, Vol. 67, No. 4, 2022, pp. 1497-1501.

12. S. Niknafs, D. Phelan, R. Dippenaar, “High-temperature laser-scanning confocal microscopy as a tool to study the interface instability during unsteady-state solidification of low-carbon steel,” *Journal of Microscopy,* Vol. 249, 2013, pp. 53-61.

13. Wilfried Kurz, “Plane Front Solidification,” *ASM Handbook Volume 15: Casting*, Materials Park, O.H., USA: ASM International, 2008, pp. 293-298.

14. J.R. Davis, “Solidification of Metals and Alloys,” *Metals Handbook Desk Edition, Second Edition*, Materials Park, O.H., USA, ASM International, 1998, pp. 728-735.

15. Philipp Dorrer, Susanne K. Michelic, Christian Bernhard, Alexander Penz, and Roman Rossler, “Study on the Influence of FeTi-Addition on the Inclusion Population in Ti-Stabilized ULC Steels and Its Consequences for SEN-Clogging,” *Steel Research International*, Vol. 90, 2019, pp. 1800635-1800635.

16. Katsunari Oikawa, Hiroshi Ohtani, Kiyohito Ishida, Taiji Nishizawa, “The Control of the Morphology of MnS Inclusions in Steel during Solidification,” *ISIJ International*, Vol. 35, No. 4, 1995, pp. 402-408.

17. Minggang Li, Hiroyuki Matsuura, Fumitaka Tsukihashi, “Evolution of Al-Ti Oxide Inclusion during Isothermal Heating of Fe-Al-Ti Alloy at 1573 K (1300°C),” *Metallurgical and Materials Transactions B*, Vol. 48, 2017, pp. 1915-1923.

